Journal of Hazardous Materials 389 (2020) 122137

Contents lists available at ScienceDirect

Journal of Hazardous Materials

journal homepage: www.elsevier.com/locate/jhazmat

Persulfate activation by two-dimensional MoS_2 confining single Fe atoms: Performance, mechanism and DFT calculations

Li-Zhi Huang[a], Chu Zhou[a], Miaolong Shen[a], Enlai Gao[a], Chunbo Zhang[a], Xin-Ming Hu[b], Yiqun Chen[a,*], Yingwen Xue[a], Zizheng Liu[a,*]

[a] School of Civil Engineering, Wuhan University, No. 8, East Lake South Road, Wuhan 430072, China
[b] Carbon Dioxide Activation Center, Interdisciplinary Nanoscience Center (iNANO) and Department of Chemistry, Aarhus University, Gustav Wieds Vej 14, DK-8000, Aarhus C, Denmark

GRAPHICAL ABSTRACT

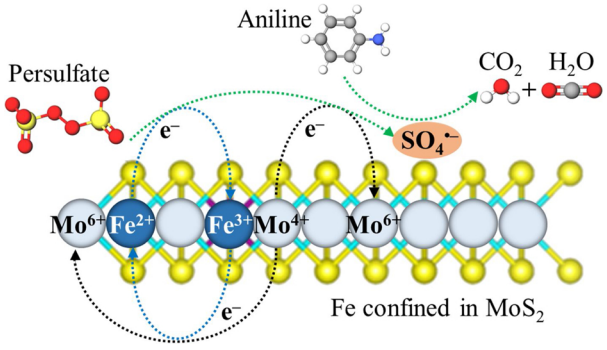

ARTICLE INFO

Editor: Xiaohong Guan

Keywords:
Persulfate activation
Co-catalysis
Single-atom catalyst
Advanced oxidation process

ABSTRACT

Developing efficient catalysts for persulfate (PS) activation is important for the potential application of sulfate-radical-based advanced oxidation process. Herein, we demonstrate single iron atoms confined in MoS_2 nanosheets with dual catalytic sites and synergistic catalysis as highly reactive and stable catalysts for efficient catalytic oxidation of recalcitrant organic pollutants *via* activation of PS. The dual reaction sites and the interaction between Fe and Mo greatly enhance the catalytic performance for PS activation. The radical scavenger experiments and electron paramagnetic resonance results confirm and $SO_4^{\cdot -}$ rather than $HO^{\cdot}$ is responsible for aniline degradation. The high catalytic performance of $Fe_{0.36}Mo_{0.64}S_2$ was interpreted by density functional theory (DFT) calculations *via* strong metal-support interactions and the low formal oxidation state of Fe in $Fe_xMo_{1-x}S_2$. $Fe_xMo_{1-x}S_2$/PS system can effectively remove various persistent organic pollutants and works well in a real water environment. Also, $Fe_xMo_{1-x}S_2$ can efficiently activate peroxymonosulfate, sulfite and H_2O_2, suggesting its potential practical applications under various circumstances.

1. Introduction

Developing technologies for efficient removal of persistent organic pollutants is strongly desired during water treatment and wastewater reclamation process. Advanced oxidation processes (AOPs) are believed as one of the most promising technologies to obtain this goal. Hydroxyl

* Corresponding authors.
E-mail addresses: yq.chen@whu.edu.cn (Y. Chen), lzz2015@whu.edu.cn (Z. Liu).

https://doi.org/10.1016/j.jhazmat.2020.122137
Received 15 October 2019; Received in revised form 14 January 2020; Accepted 18 January 2020
Available online 18 January 2020
0304-3894/ © 2020 Elsevier B.V. All rights reserved.

radical ($HO^{\cdot}$), which is highly reactive towards nearly all persistent organic pollutants, is the most used oxidants generated from ozone or H_2O_2 in AOPs. Using ozone as a $HO^{\cdot}$ source require complex and high-cost ozone generation system which hinders its large scale application (Lee et al., 2017). H_2O_2 generate $HO^{\cdot}$ *via* Fenton process ($Fe^{2+} + H_2O_2 \rightarrow Fe^{3+} + HO^{\cdot} + OH^{-}$), which requires acidic pH (Chakma and Moholkar, 2014). Thus, a large amount of acid and base is needed for pH adjustment. Sludge production and disposal during Fenton process is also a great environmental concern (Zeng et al., 2019).

Sulfate radical ($SO_4^{\cdot -}$) has been recently recognized as one of the most highly reactive oxidants, as superior as hydroxyl radical ($HO^{\cdot}$), for degradation of organic pollutants in AOPs. Persulfate (PS) has been widely utilized as a precursor to generate sulfate radicals. PS can be activated *via* various catalysts, alkaline, heat, UV irradiation and electrochemical method to generate $SO_4^{\cdot -}$ (Ahmad et al., 2013; Johnson et al., 2008; Furman et al., 2010; Kim et al., 2018; Matzek et al., 2018). In contrast to the high energy consumption and high chemical dosage for most of these activation methods, transitional metal-based catalyst has been proved to be efficient and cost-effective to activate PS in potential practical applications (Zhang et al., 2013). Transitional metal ions dissolved in homogeneous solutions are one type of efficient catalysts for PS activation (Huang and Huang, 2009). Unfortunately, the formation of metal sludge and the potential health hazards caused by free metal ions in water is of great concern. Thus, a variety of metal nanomaterials have been developed and used as heterogeneous catalysts for the activation of PS (Rong et al., 2019; Xu et al., 2019; Zhou et al., 2019; Liu et al., 2014). Metal nanomaterials are relatively stable for catalysis and can be reused after separation from the treated water. However, the low activity is always the issue compared to homogeneous metal ions (Zhang et al., 2018). The intrinsic reason is that PS activation only occurs on the surface of metal nanomaterials, and any metal atoms inaccessible by PS molecules are not involved in the catalytic process. Single-atom catalysts (SACs), with atomically distributed active sites on supports, are believed to have the advantages of both homogeneous catalysts (high reactivity) and heterogeneous catalysts (stable, easy to separate and reuse, no secondary pollution) in water treatment applications (Chen et al., 2018). Application of SACs in AOPs has been scarcely studied although it is one of the most promising strategies to maximize the efficiency of AOPs in potential practical applications (Li et al., 2018; Guo et al., 2019; Yin et al., 2019; An et al., 2018).

The surface free energy is extremely high for SACs, thus the aggregation of SACs is a big problem during their application. This problem can be solved by anchoring single metal atoms on suitable catalyst support (Zhang et al., 2018). Various supports have been developed to confine SACs, including 3D (carbon, metal oxide, MoC, metal-organic frameworks etc.) and 2D supports (graphene, g-C_3N_4, and MoS_2) (Lin et al., 2013; Pei et al., 2015; Qiu et al., 2015; Yan et al., 2015; Jones et al., 2016; Li et al., 2016; Liu et al., 2016; Yin et al., 2016; Wang et al., 2019; Sun et al., 2019). SACs confined in 2D supports have several unique features compared to 3D supports such as more coordinatively unsaturated single atoms, expedited mass-transfer on both sides of the 2D structure, and the well-defined 2D motif allowing catalytic performances interpreted theoretically (Wang et al., 2019). Also, the interaction between SACs and supports significantly influence the activity, selectivity, and stability of the catalysts (Zhang et al., 2018). Recent studies have shown that MoS_2 can act as co-catalyst in homogeneous Fenton-like reaction (Xing et al., 2018; Liu et al., 2018). Thus, we hypothesize that Fe SACs confined in 2D MoS_2 support may lead to strong SACs-supports interaction and lead to high activity in AOPs.

In this work, we report the in-plane doping of single Fe atoms in 2D MoS_2 with various Fe content (designated as $Fe_xMo_{1-x}S_2$) and demonstrate that $Fe_xMo_{1-x}S_2$ is a highly active catalyst for PS activation, thereby leading to complete mineralization of aniline, a persistent organic pollutant widely detected in surface and ground waters. The high activity of $Fe_xMo_{1-x}S_2$ derives from the synergistic catalysis between the atomically distributed Fe and Mo sites, as revealed by experiments and theoretical calculations. Sulfate radicals are demonstrated to be the major reactive oxygen species responsible for the oxidative degradation of aniline. Furthermore, the $Fe_xMo_{1-x}S_2$/PS system can degrade a wide range of other persistent organic pollutants and work well in a real water environment, testifying the great potential of $Fe_xMo_{1-x}S_2$/PS system for practical water treatment applications.

2. Materials and methods

2.1. Chemicals and materials

The $Fe_xMo_{1-x}S_2$ nanosheets were synthesized *via* a biomolecule-assisted hydrothermal synthetic route (Chang and Chen, 2011; Miao et al., 2015). $FeSO_4{\cdot}7H_2O$, $Na_2MoO_4{\cdot}2H_2O$, and L-cysteine were used as iron, molybdenum and sulfur source, respectively. A 200 mL aqueous solution consists of $Na_2MoO_4{\cdot}2H_2O$, $FeSO_4{\cdot}7H_2O$ and L-cysteine were used as a precursor for hydrothermal synthesis. The $Fe_xMo_{1-x}S_2$ with different x was synthesized by varying $Na_2MoO_4{\cdot}2H_2O/FeSO_4{\cdot}7H_2O$ ratios of 1/1, 1/3 and 3/1 with the sum of molar amounts at 12.5 mM. The concentration of L-cysteine was 66 mM for all the synthesis. MoS_2 was synthesized using 12.5 mM $Na_2MoO_4{\cdot}2H_2O$ and 66 mM L-cysteine, and FeS catalyst was synthesized using 12.5 mM $FeSO_4{\cdot}7H_2O$ and 66 mM L-cysteine. The synthesis was carried out in a 300 mL autoclave at 200 °C for one day. The as-synthesized $Fe_xMo_{1-x}S_2$ catalyst was thoroughly washed with 1 M H_2SO_4, Milli-Q water and ethanol (EtOH) *via* filtration/re-suspension to remove any unreacted residual salts. Finally, the washed catalysts were dried in an oven at 65 °C and stored in a desiccated vessel at inert atmosphere until further use.

2.2. Catalytic reactions

Degradation of aniline and other selected organic pollutants were carried out to evaluate the catalytic performance of $Fe_xMo_{1-x}S_2$/PS system. The concentration of organic pollutants was 10 μM and a catalyst dosage of 0.01-0.2 g/L was used. The PS, peroxymonosulfate, sulfite and H_2O_2 stock solution was always freshly prepared. The initial reaction pH was adjusted to 3–8 using NaOH and HCl solutions. The reaction was initiated by adding $0.1-2$ mM sulfite or peroxide. Once the degradation was initiated, 2 mL samples were withdrawn from the reaction suspensions at given time intervals and immediately quenched by 50 μL EtOH. The quenched sample was filtered and analyzed by a high-performance liquid chromatography (HPLC, 1220 Infinity II, Agilent, U.S.A). For the reuse of the catalyst, the catalysts were collected by filtration at the end of each experiment, washed 2–3 times with ultrapure water and EtOH, vacuum dried, and then used for the next cycle.

2.3. Analytical methods

Aniline, Orange II, Estriol (E3), benzoic acid, p-chlorobenzoic acid, nitrobenzene and propranolol were determined using HPLC equipped with a C18 column. The analytical conditions including mobile phase composition, wavelength, and retention time are shown in Table S1. Orange II was determined using a photospectrometer at wavelengths of 485 nm. The degradation products of aniline were determined by gas chromatography-mass spectrometry (GC–MS, QP2010, Shimadzu, Japan). Total organic carbon (TOC) analysis was performed on a TOC analyzer (Analytik Jena multi N/C 2100). Samples were pre-concentrated *via* freeze drying followed by TOC determination. X-ray photoelectron spectra (XPS) were obtained using a Kratos Axis Ultra^{DLD} instrument, and all binding energies were calibrated to adventitious C (284.8 eV). High-resolution transmission electron microscopy (HRTEM) and high-angle annular dark-field scanning transmission electron microscopy (HAADF-STEM) images were obtained using an image spherical aberration-corrected TEM system (FEI Titan 60-300) with an

accelerating voltage of 300 kV. Scanning electron microscopy (SEM) images were observed by a Quanta 200 microscope (FEI Company, USA) operating at 10 kV. X-ray diffraction (XRD) data was obtained by using a Malvern Panalytical X-ray diffractometer (XPert Pro). The possible reactive radicals produced in the system were identified by electron paramagnetic resonance (ESR), and 5,5-dimethyl-1-pyrroline N-oxide (DMPO) was used as a spin trapping agent.

2.4. Theoretical calculations

Density functional theory (DFT) calculations were performed by using the Vienna *Ab*-initio simulation package (VASP) (Kresse and Hafner, 1994; Kresse and Furthmüller, 1996). The ion-electron interactions were described by the projector augmented wave potential (Blöchl, 1994). General gradient approximation is used as the exchange and correlation functional parameterized by Perdew, Burke, and Ernzerhof (Perdew et al., 1996). The plane-wave basis sets with an energy cutoff of 520 eV and the *k*-point densities > 20 Å in the reciprocal space were used in all calculations (Monkhorst and Pack, 1976). For structural relaxation, the force on each atom is converged below 0.01 eV $Å^{-1}$. To avoid periodic image interaction, a vacuum separation of 30 Å was used to isolate the system.

3. Results and discussions

3.1. Experimental and theoretical characterization of $Fe_xMo_{1-x}S_2$

STEM images show $Fe_xMo_{1-x}S_2$ has a nanosheet morphology similar to MoS_2 (Fig. 1a). No nanoparticles or distinct clusters can be observed by TEM, implying impurities such as ferrous sulfide does not exist in $Fe_xMo_{1-x}S_2$. EDS elemental mapping in HAADF-STEM images demonstrates the homogeneous distribution of Fe, Mo, and S in the $Fe_xMo_{1-x}S_2$ nanosheets (Fig. 1b-d). The atomically dispersion of Fe atoms in MoS_2 matrix was evidenced by the dispersed white dots in the MoS_2 matrix observed by spherical aberration–corrected HRTEM. These white dots could be assigned as single Fe atoms (Fig. 1e). The relative low contrast observed in our work compared to Pt or Pd doped MoS_2 is attributed to the small difference of atomic numbers between Fe and Mo (Deng et al., 2015; Luo et al., 2018). The HRTEM image shows distinct ripples and corrugations which is typical for MoS_2 (Huang et al., 2017). The observed layer spacing (~0.67 nm) corresponding to the (002) plane is slightly larger than that of standard MoS_2 (~0.62 nm) (Fig. 1f). A similar observation of enlarged interlayer spacing was reported with Ni-doped MoS_2 (Miao et al., 2015).

To explore the stability of $Fe_xMo_{1-x}S_2$ catalyst, we calculated the formation energy of the Fe-doped systems. The formation energy of the $Fe_xMo_{1-x}S_2$ is calculated by

$$\Delta E_f = E_{Fe_xMo_{1-x}S_2} + xE_{Mo} - (E_{MoS_2} + xE_{Fe}) \quad (1)$$

where $E_{Fe_xMo_{1-x}S_2}$ and E_{MoS_2} are the energy of $Fe_xMo_{1-x}S_2$ and MoS_2 per formula unit, respectively. E_{Mo} and E_{Fe} is the energy of per Mo and Fe in bulk form, respectively. The formation energy of $Fe_xMo_{1-x}S_2$ was plotted as shown in Fig. 2, indicating that the decreasing stability of $Fe_xMo_{1-x}S_2$ as the Fe-doping concentration increases.

3.2. Catalytic performance

The oxidative degradation of aniline was investigated to evaluate the performance of the $Fe_xMo_{1-x}S_2$ catalyst for PS activation (Fig. 3a). The removal of aniline was negligible in the presence of only $Fe_{0.36}Mo_{0.64}S_2$ or PS, excluding the possibility that $Fe_{0.36}Mo_{0.64}S_2$ or PS alone is capable of degrading aniline. Hence, it is the activation of PS catalyzed by $Fe_{0.36}Mo_{0.64}S_2$ that is responsible for aniline degradation in all our studied systems. Using pristine MoS_2 as a catalyst, the aniline degradation is slow and not complete in 60 min, indicating the moderate activity of the pristine MoS_2 for PS activation. The Fe2p and S2p spectra of the as-synthesized FeS suggest that Fe has the oxidation state of +2 and S has the oxidation state of −2 (Figure S1), which are the same as in $Fe_{0.36}Mo_{0.64}S_2$. However, the catalytic performance of FeS is even worse than MoS_2, with only 14 % of aniline removed after 60 min. The doping of Fe sites in MoS_2 significantly accelerates the aniline removal. The removal efficiency increases with the Fe content in $Fe_xMo_{1-x}S_2$ and is saturated at $x = 0.36$, demonstrating the important roles of both Fe and Mo sites in $Fe_xMo_{1-x}S_2$, probably acting synergistically in catalytic PS activation. Also, too high Fe content lower the structural stability of $Fe_xMo_{1-x}S_2$ as demonstrated by the theoretical calculation. Thus, $Fe_{0.36}Mo_{0.64}S_2$ was regarded as the optimum catalyst and used in the following experiments.

In the system of $Fe_{0.36}Mo_{0.64}S_2$/PS, aniline was removed completely within only 20 min (Fig. 3a). Moreover, total organic carbon (TOC) disappeared within the same period (Fig. 3b), which is in line with the aniline degradation curves and indicates the complete mineralization of aniline to CO_2 and H_2O. The higher standard error in TOC measurement compared with aniline mearsument could be attributed to the low aniline concentration (10 μM) and the uncertainties due to evaporation of aniline during the freeze drying process. In contrast, no obvious aniline degradation was observed in the MoO_3/PS, Fe_2O_3/PS, and Fe_3O_4/PS systems (Fig. 3c). These results suggest the high activity of $Fe_{0.36}Mo_{0.64}S_2$ for PS activation, leading to efficient pollutant degradation.

We observed the gradual leaching of Fe and Mo ions into solution while using $Fe_{0.36}Mo_{0.64}S_2$ for PS activation (Figure S2a). After 20 min, a period for the complete aniline degradation, 1.18 mg/L of Mo and 1.16 mg/L of Fe ions were detected in the solution, corresponding to ~1 % of the dosage of $Fe_{0.36}Mo_{0.64}S_2$ catalyst. Using such concentration of Mo ions to catalyze homogeneously PS activation results in negligible aniline gradation, while in the case of 1.16 mg/L of Fe, ~20 % of aniline degraded after 20 min, significantly lower than the aniline degradation efficiency (100.0 %) observed in $Fe_{0.36}Mo_{0.64}S_2$/PS system (Figure S2b). In reality, the concentrations of Fe and Mo ions are lower than these numbers during the reaction course catalyzed by $Fe_{0.36}Mo_{0.64}S_2$, which hints that even less aniline degrades *via* homogeneous activation of PS. Thus, the homogenous PS activation by leached Fe and Mo ions has only a small contribution to aniline degradation compared with heterogeneous PS activation by $Fe_{0.36}Mo_{0.64}S_2$. Our further investigations found that the dissolved Fe combines with MoS_2 or $Fe_xMo_{1-x}S_2$ could enhance the activation of PS (Figure S3). It suggest that MoS_2 or $Fe_xMo_{1-x}S_2$ act as co-catalyst during the activation of PS by Fe^{2+}. Similarly, MoS_2 has been reported as co-catalyst during Fenton reaction, i.e. the activation of H_2O_2 by Fe^{2+}, in previous publications (Xing et al., 2018; Liu et al., 2018). MoS_2 could facilitate the rate-limiting step in Fenton process (reduction of Fe^{3+} to Fe^{2+}) *via* reaction ($Fe^{3+} + Mo^{4+} \rightarrow Fe^{2+} + Mo^{6+}$). This co-catalytic mechanism is similar to ours except that the Fe^{3+}/Fe^{2+} and Mo^{4+}/Mo^{6+} redox cycle occur within the two-dimensional MoS_2 structure in our work (see below). Although dissolved Fe combines with MoS_2 and $Fe_xMo_{1-x}S_2$ could enhance the activation of PS, the concentration of Fe in reaction solution is still relatively high which may result in secondary pollution and sludge formation. Our results demonstrate that doping of MoS_2 with single Fe atoms could convert the homogeneous catalytic system to heterogeneous one. The concentration of Fe ions in reaction solution can thus be significantly lowered while retaining the high catalytic performance in homogeneous system.

In order to investigate the reusability of the $Fe_{0.36}Mo_{0.64}S_2$ catalyst, the catalyst was recycled five times and the catalytic performance was evaluated (Fig. 3d). During the first four cycles, the degradation efficiency of aniline was all above 80 %. The degradation efficiency of aniline was still about 50 % in the fifth cycles. It indicates the relatively good reusability and stability of $Fe_{0.36}Mo_{0.64}S_2$ for PS activation. Three degradation products other than CO_2 and H_2O were observed by

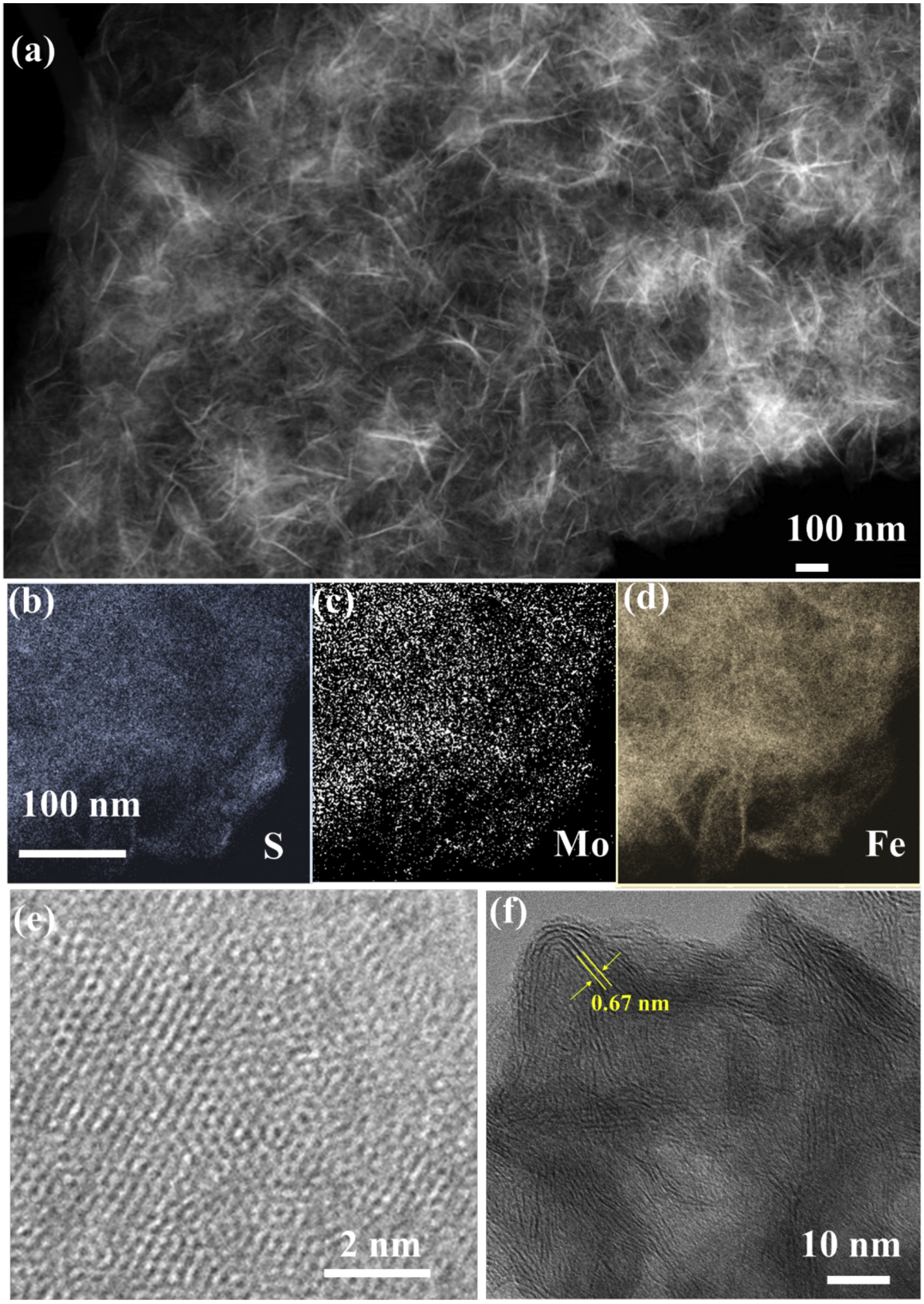

Fig. 1. Morphologic characterization of $Fe_xMo_{1-x}S_2$ (x = 0.36) catalyst. (a) STEM. (b–d) STEM-EDS chemical maps of S, Mo and Fe. (e–f) HRTEM images.

GC–MS (Figure S4). These degradation products could adsorb on the $Fe_{0.36}Mo_{0.64}S_2$ catalyst surface, which may block the active site for PS activation in the followed run. Subsequently, a decrease in catalytic performance was observed if the catalyst was reused.

3.3. Identification of radicals

The ESR signals detected in the $Fe_{0.36}Mo_{0.64}S_2$/PS system are the combination of DMPO–$SO_4^{\cdot -}$ (aN = 13.9 G, aH = 10 G, aH = 1.48 G,

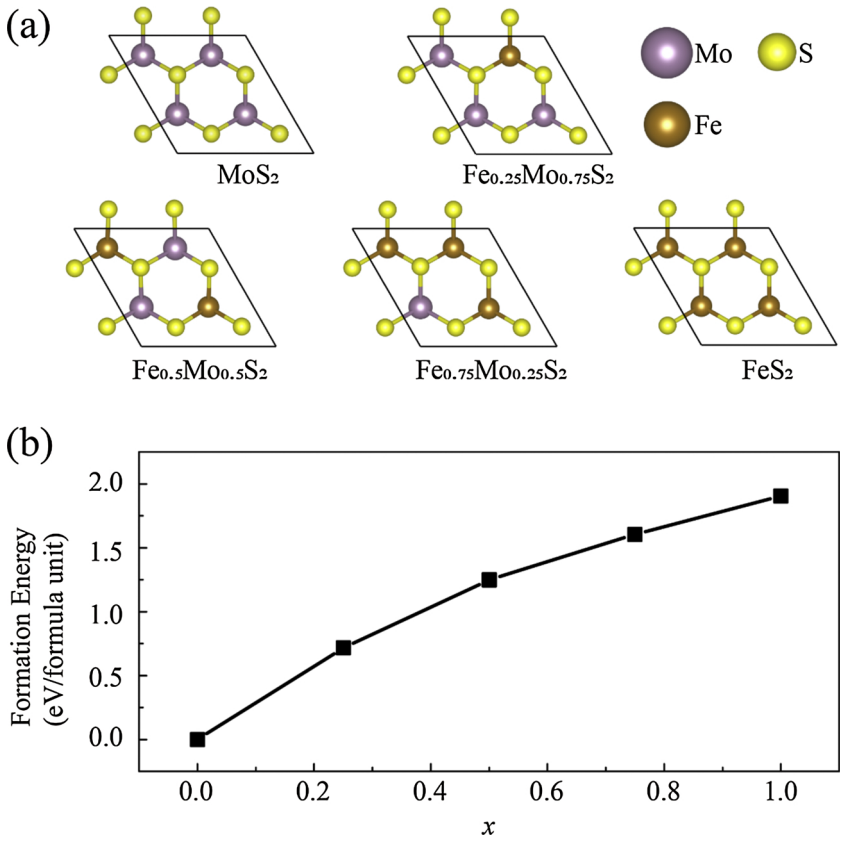

Fig. 2. Theoretical characterization of $Fe_xMo_{1-x}S_2$ catalyst. (a) Illustration of $Fe_xMo_{1-x}S_2$ with varying Fe-doping concentration (x = 0.00, 0.25, 0.50, 0.75 and 1.00). (b) Corresponding formation energy as a function of x.

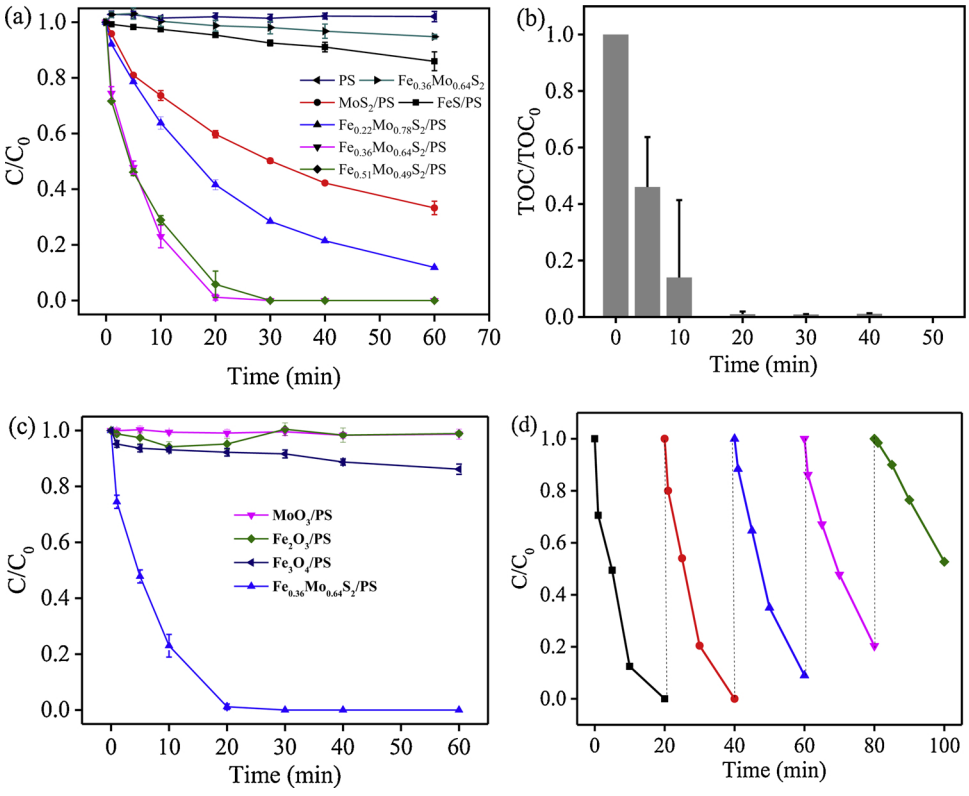

Fig. 3. Catalytic performance of $Fe_xMo_{1-x}S_2$ for PS activation. (a) Aniline degradation in $Fe_xMo_{1-x}S_2$/PS systems. (b) Change of total organic carbon during aniline degradation in $Fe_{0.36}Mo_{0.64}S_2$/PS system. (c) Aniline degradation in different systems. (d) Reuse of $Fe_{0.36}Mo_{0.64}S_2$ catalyst in $Fe_{0.36}Mo_{0.64}S_2$/PS system. $[Aniline]_0$ = 10 μM, $[PS]_0$ = 1 mM, catalyst dosage = 0.1 g/L, pH = 4.0.

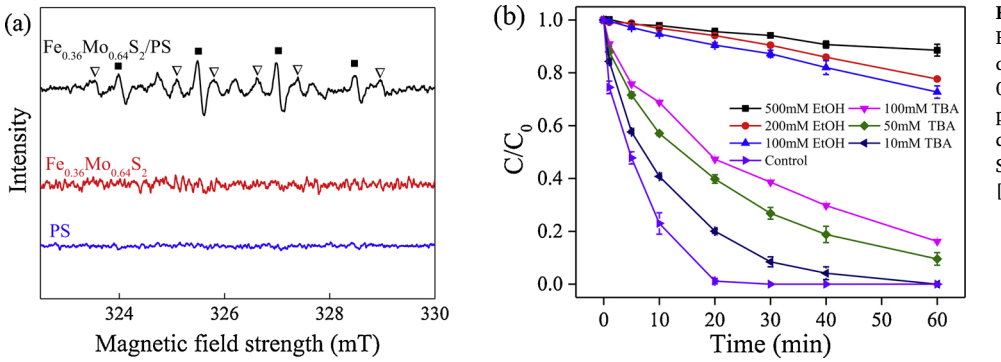

Fig. 4. Identification of radicals in $Fe_{0.36}Mo_{0.64}S_2$/PS system. (a) Radical quenching experiments. $[Fe_{0.36}Mo_{0.64}S_2]_0$ = 0.1 g/L, $[Aniline]_0$ = 10 μM, $[PS]_0$ = 1 mM, pH = 4.0. (b) ESR signal under different conditions. (■): DMPO – $HO^{\cdot}$ adduct, (▽): DMPO-$SO_4^{\cdot -}$ adduct. $[Fe_{0.36}Mo_{0.64}S_2]_0$ = 0.1 g/L, $[PS]_0$ = 1 mM, $[DMPO]_0$ = 100 mM, pH 4.

aH = 0.78 G) and DMPO–$HO^{\cdot}$ (aN = aH = 14.9 G) (Fig. 4a). Thus, it can be concluded $SO_4^{\cdot -}$ and $HO^{\cdot}$ were generated in $Fe_{0.36}Mo_{0.64}S_2$/PS system. In order to understand which type of radicals play the major role in aniline degradation, EtOH and tert-butanol (TBA) were selected as scavengers to quench radicals in the system. In the presence of 100 mM TBA as $HO^{\cdot}$ scavenger 10,000 times of aniline concentration, the aniline degradation efficiency is as high as 83.8 % after 60 min reaction (Fig. 4b). It demonstrates $HO^{\cdot}$ has little contribution to aniline degradation. In contrast, the aniline degradation efficiency was only 27.3 %, 23.4 % and 11.4 % with the addition of 100 mM, 200 mM and 500 mM EtOH, respectively (Fig. 4b). Therefore, it is suggested that $SO_4^{\cdot -}$ rather than $HO^{\cdot}$ is mainly responsible for aniline degradation in $Fe_{0.36}Mo_{0.64}S_2$/PS system.

3.4. Influence of reaction parameters

Effect of pH, PS concentration, and $Fe_{0.36}Mo_{0.64}S_2$ dosage on aniline degradation in $Fe_{0.36}Mo_{0.64}S_2$/PS system have been investigated. A general trend was observed that the PS activation by $Fe_{0.36}Mo_{0.64}S_2$ is more efficient under acidic conditions than under neutral or alkaline conditions (Fig. 5a), and the pH variation during reaction is shown in Figure S5. The highest aniline degradation rate was observed at pH = 4.0 with an initial degradation rate r_0 of 0.71 μM/min. This phenomenon is probably due to the different active sites on the catalyst surface and different aniline species under varying pH conditions (Figure S6). Firstly, Fe species on the surface of $Fe_{0.36}Mo_{0.64}S_2$ may be protonated and mainly exist as > Fe-$(H_3O)_m^{n+}$ (> denotes the catalyst surface) during reaction at pH 4.0. A positively charged catalyst surface is prone to attract the negatively charged $S_2O_8^{2-}$ *via* electrostatic interaction, which favors the electron transfer between > Fe-$(H_3O)_m^{n+}$ and $S_2O_8^{2-}$. When pH increases to near neutral, the Fe species on $Fe_{0.36}Mo_{0.64}S_2$ catalyst may exist as > Fe-$(H_2O)_m$. The less positively-charged or neutral catalyst surface weakens the electrostatic attraction between $Fe_{0.36}Mo_{0.64}S_2$ and $S_2O_8^{2-}$. When pH further increased to alkaline conditions, Fe becomes negatively charged > Fe-$(OH)_m^{n-}$ surface complex. The possible electrostatic repulsion between > Fe-$(OH)_m^{n-}$ and $S_2O_8^{2-}$ inhibited the contact between $Fe_{0.36}Mo_{0.64}S_2$ and PS, unfavoring the subsequent radical production for aniline degradation. Secondly, aniline becomes protonated at pH < 4.6 (pKa = 4.6). The electrostatic attraction between the positively charged aniline

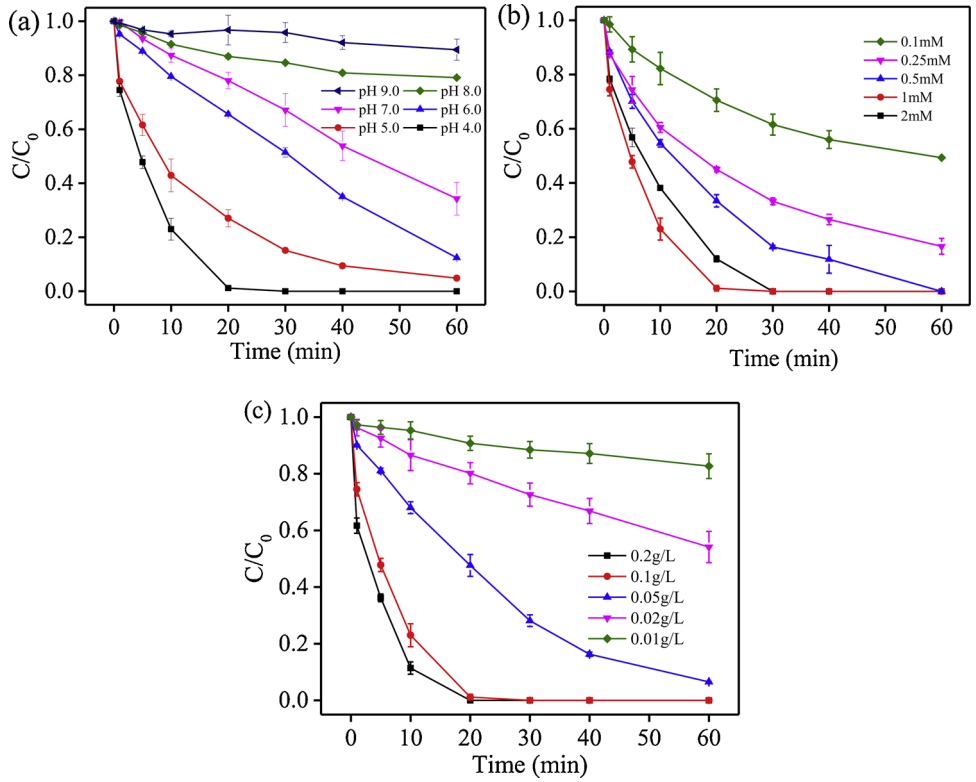

Fig. 5. Influence of reaction parameters on aniline degradation in $Fe_xMo_{1-x}S_2$/PS system. (a) pH. (b) PS concentration. (c) $Fe_{0.36}Mo_{0.64}S_2$ dosage. $[Aniline]_0$ = 10 μM, $Fe_{0.36}Mo_{0.64}S_2$ dosage = 0.1 g/L (if needed), $[PS]_0$ = 1 mM (if needed), pH = 4.0 (if needed).

molecules and the negatively charged $S_2O_8^{2-}$ may favor the aniline degradation at pH 4. It should be noted that the effect of pH variation (from pH 4.0 to 9.0) on the MoS_2 catalyzed PS activation is limited as reported by a recent publication (Zhou et al., 2020). Thus, it is reasonable that the effect of pH variation on $Fe_xMo_{1-x}S_2$/PS system was similar to the Fe catalyzed Fenton-like system.

The PS concentration also influences aniline degradation in $Fe_{0.36}Mo_{0.64}S_2$/PS system (Fig. 5b). When the concentration of PS increases from 0.1 mM to 1 mM, the aniline degradation rate increases from 0.18 μM/min to 0.71 μM/min. Further increase of the PS concentration from 1 mM to 2 mM leads to a decrease of aniline degradation rate to 0.56 μM/min. Although PS is important for radical generation in $Fe_{0.36}Mo_{0.64}S_2$/PS system, excessive PS may react with $SO_4^{\cdot-}$ to form $S_2O_8^{\cdot-}$ with low oxidative capability (Reaction 2). A too high concentration of PS results in the competition between PS and aniline for $SO_4^{\cdot-}$, unfavoring the aniline degradation in $Fe_{0.36}Mo_{0.64}S_2$/PS system.

$$SO_4^{\cdot-} + S_2O_8^{2-} \rightarrow SO_4^{2-} + S_2O_8^{\cdot-} \quad k = 5.5 \times 10^5\ M^{-1}S^{-1} \quad (2)$$

Besides, the degradation efficiency of aniline increases with the $Fe_{0.36}Mo_{0.64}S_2$ dosage in $Fe_{0.36}Mo_{0.64}S_2$/PS system (Fig. 5c). The reason for this phenomenon may be that increasing the dosage of $Fe_{0.36}Mo_{0.64}S_2$ nanomaterials can provide more catalytic active sites for PS activation, thereby increasing the yield of $SO_4^{\cdot-}$ and enhancing the degradation efficiency of aniline.

3.5. Potential application and versatility of $Fe_xMo_{1-x}S_2$ catalyst

Chloride anion is abundant in natural waters. The presence of Cl^- promotes the aniline degradation indicating the high reactivity of $Fe_{0.36}Mo_{0.64}S_2$/PS system under natural environment (Fig. 6a). The possible reason for this phenomenon is that Cl^- can react with $SO_4^{\cdot-}$ to form $Cl^{\cdot}$ (Reaction 3) which form $HOCl^{\cdot-}$ subsequently (Reaction 4). The presence of $Cl^{\cdot}$ and $HOCl^{\cdot-}$ oxidative radicals can thus enhance aniline degradation.

$$SO_4^{\cdot-} + Cl^- \rightarrow Cl^{\cdot-} + SO_4^{2-} \quad k = 2.7 \times 10^8\ M^{-1}\ S^{-1} \quad (3)$$

$$Cl_2^{\cdot-} + H_2O \rightarrow HOCl_2^{\cdot-} + H^+ + SO_4^{\cdot-} \quad k = 8 \times 10^9\ M^{-1}\ S^{-1} \quad (4)$$

Furthermore, real surface water was collected from the East Lake (Wuhan, China), filtrated with 0.45 μm membrane and used in the experiment. The water quality of the sampled water is shown in Table S2. Aniline can be completely degraded in $Fe_{0.36}Mo_{0.64}S_2$/PS system within 20 min in synthetic wastewater, while the complete removal of aniline in natural water background was achieved after 60 min (Fig. 6b). The produced radicals may be consumed by various organic matter dissolved in real surface water, which may inhibit the degradation of aniline in $Fe_{0.36}Mo_{0.64}S_2$/PS system. This speculation is confirmed by our experimental observation that humic acid (a chemical produced by decaying plants) can inhibit aniline degradation in $Fe_{0.36}Mo_{0.64}S_2$/PS system (Figure S7).On the other hand, the degradation of aniline in the real water was accelerated if the PS concentration was increased from 1 mM to 2 mM (Fig. 6b), even faster than that with 1 mM PS in synthetic wastewater. This is because PS with sufficient concentration can produce sufficient radicals for both aniline and various dissolved organic matter in natural water. Therefore, high degradation efficiency of organic pollutants in real polluted water may be obtained by increasing the PS dosage.

To explore the potential practical application of $Fe_xMo_{1-x}S_2$/PS system in the degradation of various organic pollutants, six target pollutants, i.e. orange II, estriol, benzoic acid, p-chlorobenzoic acid, nitrobenzene and propranolol, were chosen as target pollutants. Orange II is a non-biodegradable dye pollutant in dying industrial wastewater causing serious environmental pollution. Estriol is a widely used estrogen, which interferes with the endocrine function of organisms. Benzoic acid, p-chlorobenzoic acid and nitrobenzene are extensively used in the chemical industry, which are persistent organic pollutants widely found in the environment. Propranolol is a cardiovascular active pharmaceutical ingredient. As an emerging organic pollutant, propranolol is widely detected in surface waters. All these organic pollutants can be efficiently removed (Fig. 6c), demonstrating the great potential of $Fe_xMo_{1-x}S_2$/PS system in practical water treatment.

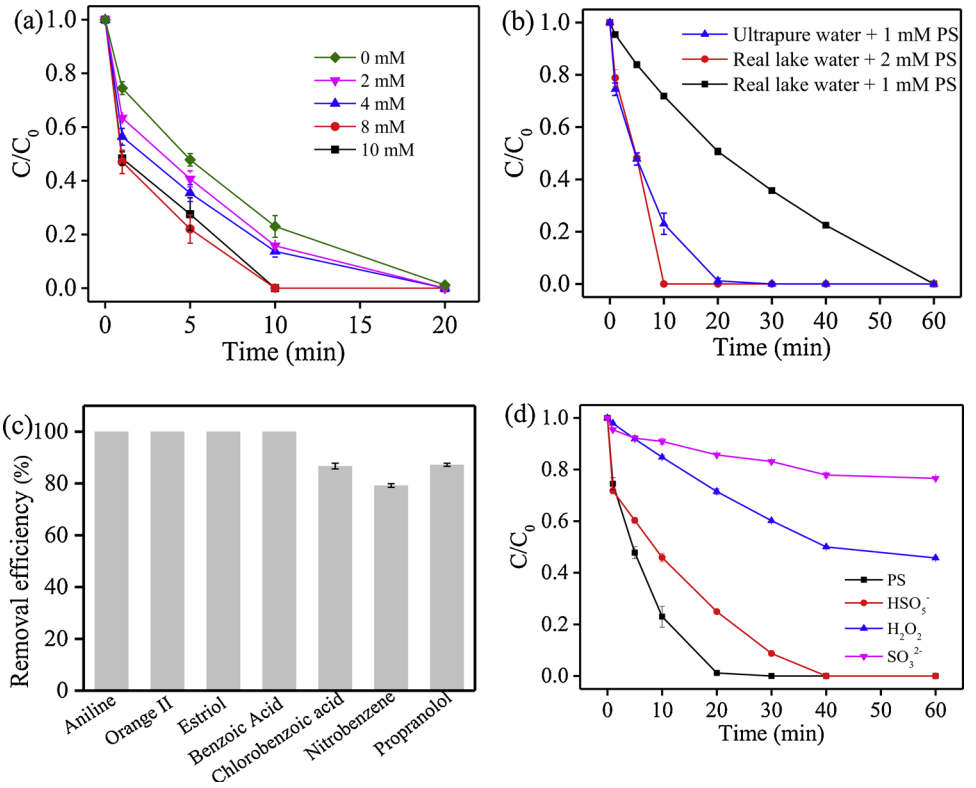

Fig. 6. Potential practical application and versatility of $Fe_xMo_{1-x}S_2$ catalyst. (a) Influence of nature abundant Cl^- ions on aniline degradation in $Fe_{0.36}Mo_{0.64}S_2$/PS system. (b) Aniline degradation by $Fe_{0.36}Mo_{0.64}S_2$/PS in real lake water. (c) Removal efficiency of various organic pollutants in $Fe_{0.36}Mo_{0.64}S_2$/PS system after 30 min reaction. (d) Application of $Fe_{0.36}Mo_{0.64}S_2$ catalyst in other advanced oxidation processes. $[Cl^-]_0$ = 0–10 mM, $[Fe_{0.36}Mo_{0.64}S_2]_0$ = 0.1 g/L, $[\text{organic pollutants}]_0$ = 10 μM, $[PS] = [HSO_5^-] = [H_2O_2] = [SO_3^{2-}]$ = 1 mM, $[\text{Aniline}]_0$ = 10 μM, pH = 4.0.

In order to further investigate the potential application of $Fe_xMo_{1-x}S_2$ in other AOP systems, aniline degradation in $Fe_{0.36}Mo_{0.64}S_2/HSO_5^-$, $Fe_{0.36}Mo_{0.64}S_2/H_2O_2$ and $Fe_{0.36}Mo_{0.64}S_2/SO_3^{2-}$ system was investigated. Aniline was completely degraded in $Fe_{0.36}Mo_{0.64}S_2/HSO_5^-$ system within 40 min, while the aniline degradation efficiency in $Fe_{0.36}Mo_{0.64}S_2/H_2O_2$ and $Fe_{0.36}Mo_{0.64}S_2/SO_3^{2-}$ system after 60 min were 54.3 % and 23.4 % respectively (Fig. 6d). The results show $Fe_xMo_{1-x}S_2$ is a versatile catalyst for most AOP systems.

3.6. Mechanism for PS activation by $Fe_xMo_{1-x}S_2$

3.6.1. Catalytic center and stability of $Fe_xMo_{1-x}S_2$

The electron transfer in $Fe_{0.36}Mo_{0.64}S_2$/PS system includes electron transfer between i) Fe and PS, ii) Mo and PS, and iii) Fe and Mo within $Fe_{0.36}Mo_{0.64}S_2$. Fe or Mo both need to be in the reduced form i.e. Fe(II) or Mo(IV) to activate PS. This is evidenced by the results that Fe_3O_4/MoS_2 rather than Fe_2O_3/MoO_3 can activate PS (Fig. 3c). Fe(II) and Mo (IV) in $Fe_{0.36}Mo_{0.64}S_2$ can both be oxidized by PS to form $SO_4^{\cdot -}$ (reaction 5–6). More importantly, > Mo(IV) can reduce > Fe(III) with the formation of > Fe(II) and > Mo(VI) (reaction 7). The Fe(II)/Fe(III) cycle is thus established, which is essential for the continuous production of $SO_4^{\cdot -}$.

$$> Fe(II) + S_2O_8^{2-} \rightarrow > Fe(III) + SO_4^{2-} + SO_4^{\cdot -} \quad (5)$$

$$> Mo(IV) + S_2O_8^{2-} \rightarrow > Mo(VI) + SO_4^{2-} + SO_4^{\cdot -} \quad (6)$$

$$> Fe(III) + > Mo(IV) \rightarrow > Fe(II) + > Mo(VI) \quad (7)$$

XPS spectra of $Fe_{0.36}Mo_{0.64}S_2$ catalyst was analyzed to further investigate the catalytic mechanism. The binding energies of the Fe $2p_{3/2}$ peak at 707.4 eV suggest most of the Fe atoms in $Fe_{0.36}Mo_{0.64}S_2$ have an oxidation state of 2+ (Fig. 7a). This exclude the presence of metallic Fe consisting of Fe-Fe bonding, which has a binding energy of 706.7 eV.

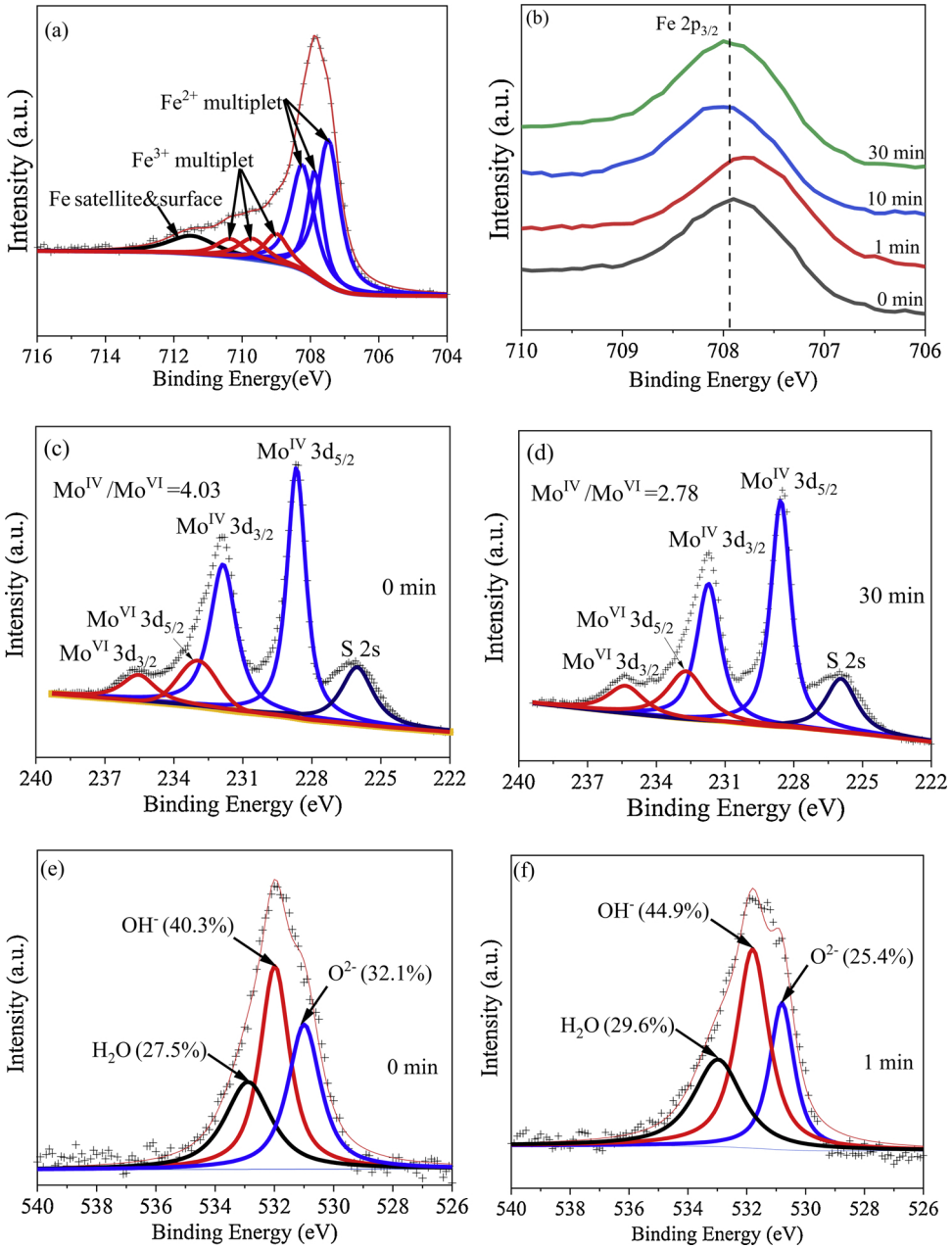

Fig. 7. Identification of catalytic center in $Fe_xMo_{1-x}S_2$ by high resolution XPS spectra along the reaction course. (a–b) Fe2p, (c–d) Mo3d and (e–f) O1 s. $[Aniline]_0$ = 10 μM, $[PS]_0$ = 1 mM, pH = 4.0, catalysts was collected and characterized after 0 min–30 min reaction.

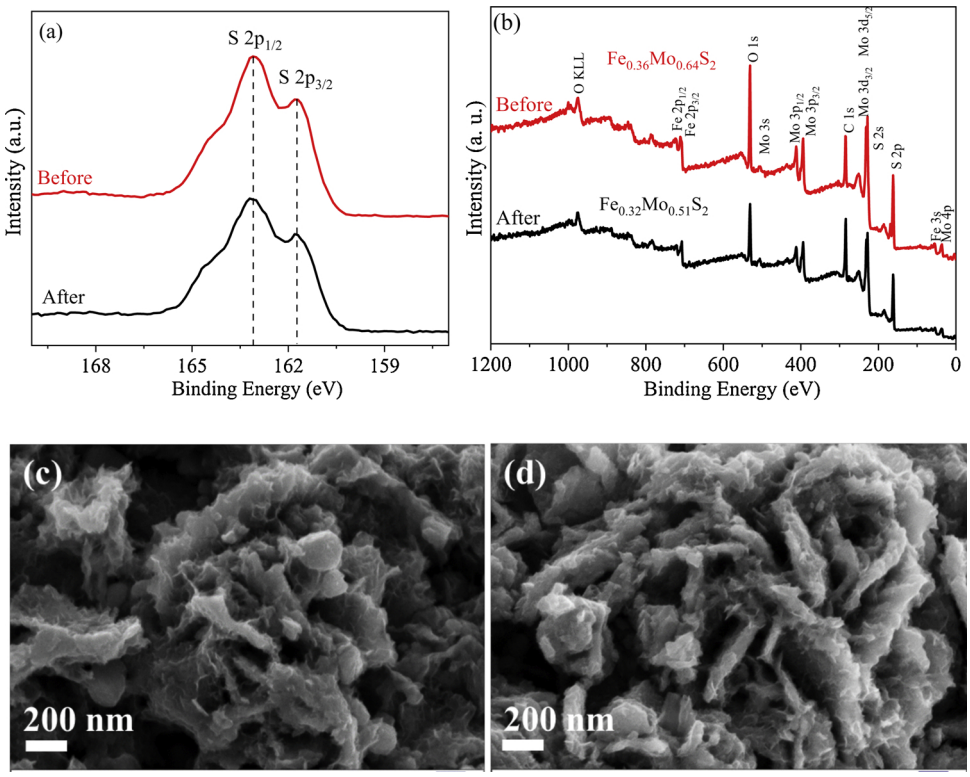

Fig. 8. Structural stability of $Fe_{0.36}Mo_{0.64}S_2$ catalyst in $Fe_{0.36}Mo_{0.64}S_2$/PS system. (a) High resolution S2p XPS spectra, (b) XPS survey spectra, (c–d) SEM images of $Fe_{0.36}Mo_{0.64}S_2$ catalyst before (c) and after (d) reaction. $[Aniline]_0$ = 10 μM, $[PS]_0$ = 1 mM, pH = 4.0, reaction time = 60 min.

The exclusion of Fe-Fe bonding suggest the atomically distribution of Fe atoms in MoS_2 matrix. The Fe $2p_{3/2}$ spectrum was fitted with closely spaced iron(II) and iron(III) multiplet peaks, and iron surface&satellite peak (Fig. 7a). The much larger areas of iron(II) multiplet peaks than areas of iron(III) multiplet peaks confirm the domination of Fe^{2+} in $Fe_{0.36}Mo_{0.64}S_2$. The position of the Fe $2p_{3/2}$ peak during the reaction has been monitored to further reveal the possible Fe redox cycle in $Fe_{0.36}Mo_{0.64}S_2$. The back and forth shifting of the Fe $2p_{3/2}$ peak position during the reaction demonstrate the cycling of Fe(II)/Fe(III) catalytic sites during reaction (Fig. 7b, reaction (5) and (7)).

The Mo3d spectrum can be fitted with two peaks at 231.9 eV and 228.7 eV for Mo(IV) $3d_{3/2}$ and Mo(IV) $3d_{5/2}$, respectively (Fig. 7c), which confirms an oxidation state of 4+ for Mo in $Fe_{0.36}Mo_{0.64}S_2$. The Mo(VI) $3d_{3/2}$ and Mo(VI) $3d_{5/2}$ peaks at 235.6 eV and 233.0 eV suggest the possible oxidation of Mo(IV) in air. The decrease of Mo^{IV}/Mo^{VI} ratio from 4.03 to 2.78 after reaction confirms the oxidation of Mo(IV) by Fe (III) and PS as shown in reaction (6) and (7) (Fig. 7 c–d). In addition, the peak at 226.2 eV is derived from S 2 s orbital (Fig. 7c).

The peak maximum of O1 s XPS spectrum at 532 eV demonstrate the valence state of O in $Fe_{0.36}Mo_{0.64}S_2$ catalyst is –2. It is reported that active oxygen species such as surface O^{2-} and OH^- play an important role in oxidation reaction. Thus high-resolution O1s spectra of $Fe_{0.36}Mo_{0.64}S_2$ catalyst during the reaction was investigated. The O1s spectra were resolved into three peaks located at 531, 532 and 533 eV which can be assigned to O^{2-}, OH^- and H_2O, respectively (Huang et al., 2013). The relative contribution of O^{2-} and OH^- changed after reaction, indicating both O^{2-} and OH^- was involved in the catalytic reaction (Fig. 7e-f). The increase of surface OH^- during reaction may result from the formation of Fe−OH groups or O_2 adsorption on $Fe_{0.36}Mo_{0.64}S_2$ surface, and the decreased O^{2-} may be oxidized by Fe^{3+} with its reduction to Fe^{2+} (Ren et al., 2015).

The two peaks at 163.1 eV and 161.7 eV observed in S2p spectra demonstrate the −2 oxidation state of S in $Fe_{0.36}Mo_{0.64}S_2$. The S 2p spectra are the same before and after the reaction (Fig. 8a). It is speculated that S^{2-} would be oxidized by PS to S^0 or SO_4^{2-}, which would release into the reaction solution. However, the involvement of S redox cycle can be excluded since there is no strong reductant in the system to reduce S^0 or SO_4^{2-} back to S^{2-}. On the other hand, the similar XPS survey spectra, the relatively constant chemical composition and morphology of the $Fe_{0.36}Mo_{0.64}S_2$ catalyst before and after reaction suggests the release of S atoms from the catalyst during reaction is negligible (Fig. 8b–d). Although the constant chemical compositions and similar SEM images may suggest the stability of the catalyst, the oxidation of Mo(IV) to Mo(VI) in the catalyst after reaction indicate the stability of the catalyst during the reaction is not excellent. The oxidation of Mo(IV) after the reaction may resulted in the declined catalytic performance of $Fe_{0.36}Mo_{0.64}S_2$ after reuse for three times (Fig. 3d). Thus, regeneration of Mo(IV) from Mo(VI) (e.g. by adding reductants) is advised to maintain the high activity during the reused of the $Fe_{0.36}Mo_{0.64}S_2$ catalyst.

3.6.2. DFT calculations

The Bader charge of Fe atom in $Fe_{0.36}Mo_{0.64}S_2$ and Mo atom in pristine MoS_2 lose 0.69 e^{-1} and 1.06 e^{-1}, respectively (Henkelman et al., 2006), indicating the amount of charge transfer of Fe in $Fe_{0.36}Mo_{0.64}S_2$ is ~35 % smaller than that of Mo in MoS_2 (Fig. 9). Moreover, after the Fe doping of MoS_2, electrons on Mo atoms and S atoms decrease ~4 % and ~6 %, respectively (Fig. 9). These results suggest the perturbation of the electronic structure of MoS_2 upon Fe doping, which may trigger the catalytic activity of MoS_2 especially for the presumably catalytic inert in-plane area of MoS_2 (Wang et al., 2019; Deng et al., 2015). The charge transfer (0.69 e^{-1}) between the confined Fe atoms and MoS_2 support indicate a strong metal-support interaction, which play an important role in preventing the single Fe atoms from aggregation (Zhang et al., 2018). Moreover, the interaction may lead to a fast charge transfer between Fe and Mo during catalysis.

The local electronic properties of the atomically distributed Fe atoms in MoS_2 support is essential for the catalytic activity of Fe. The

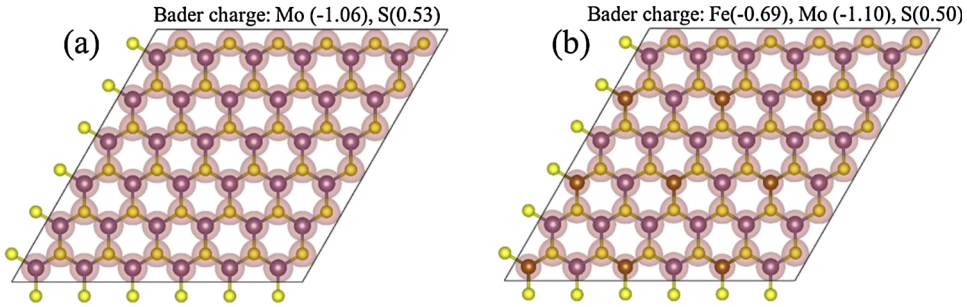

Fig. 9. Charge density and Bader charge transfer of atoms in (a) pristine MoS_2 and (b) $Fe_{0.36}Mo_{0.64}S_2$.

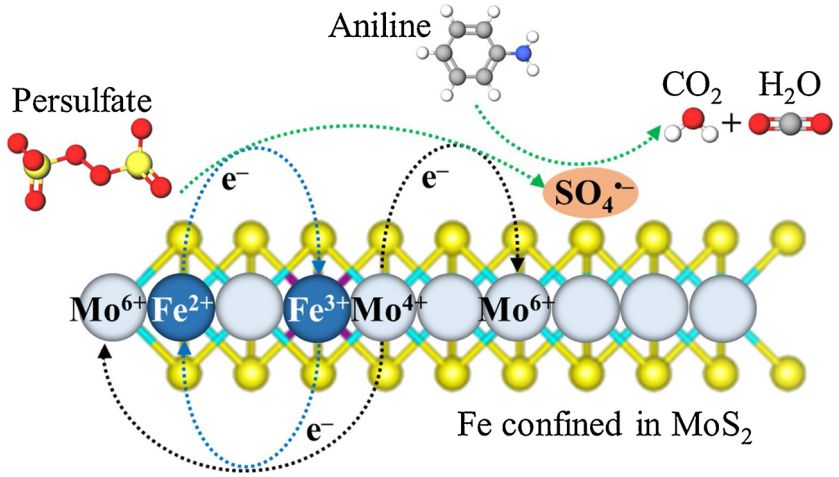

Fig. 10. Schematic illustration for the mechanism of aniline degradation in $Fe_xMo_{1-x}S_2$/PS system.

high resolution Fe2p 3/2 peak at 707.4 eV indicate a possible +2 formal oxidation state of Fe in $Fe_xMo_{1-x}S_2$ (Fig. 7b). On the other hand, the charge transfer of single Fe atoms in the local environment may differ even with similar binding energy in XPS (Raebiger et al., 2008). Thus, we compare the difference on Bader charges transfer of Fe atoms between $Fe_{0.36}Mo_{0.64}S_2$, FeO and Fe_2O_3. The charges transfer of Fe atoms follows the order of $Fe_{0.36}Mo_{0.64}S_2$ < FeO < Fe_2O_3 (Table S3), which indicate the lowest formal oxidation state of Fe in $Fe_xMo_{1-x}S_2$. This is in line with the highest reactivity of $Fe_{0.36}Mo_{0.64}S_2$ followed by Fe_3O_4 (FeO + Fe_2O_3) and Fe_2O_3 (Fig. 3c). Indeed, the low formal oxidation state of single Fe atoms possessing high reductive strength may favor the activation of PS oxidant.

Finally, the mechanism for the degradation of aniline in $Fe_xMo_{1-x}S_2$/PS system can be proposed (Fig. 10). Fe(II) and Mo(IV) in $Fe_{0.36}Mo_{0.64}S_2$ can both activate PS to form $SO_4^{\cdot -}$. More importantly, > Mo(IV) can reduce > Fe(III) to > Fe(II) for the continued production of $SO_4^{\cdot -}$. The generated highly oxidative $SO_4^{\cdot -}$ can effectively mineralize aniline to CO_2 and H_2O.

4. Conclusion

Two-dimensional MoS_2 confining single Fe atoms ($Fe_xMo_{1-x}S_2$) was synthesized to activate PS for aniline degradation. Aniline can be complete mineralized to CO_2 and H_2O as confirmed by the TOC analysis. $Fe_{0.36}Mo_{0.64}S_2$ shows good reusability and stability during PS activation. $Fe_xMo_{1-x}S_2$/PS system can effectively remove various persistent organic pollutants and $Fe_xMo_{1-x}S_2$ show high reactivity in most AOP systems. The slightly decreased degradation efficiency of aniline in real polluted water can be compensated by increasing PS dosage. The PS activation by $Fe_{0.36}Mo_{0.64}S_2$ is more efficient at acidic conditions than at neutral and alkaline conditions. The radical scavenger experiments and ESR results confirm the production of $SO_4^{\cdot -}$ and $HO^{\cdot}$ radicals, and $SO_4^{\cdot -}$ rather than $HO^{\cdot}$ is responsible for aniline degradation. It was found that the Fe and Mo catalytic sites in $Fe_xMo_{1-x}S_2$ act synergistically in catalytic PS activation. Fe(II) and Mo(IV) in $Fe_{0.36}Mo_{0.64}S_2$ can both activate PS to form $SO_4^{\cdot -}$. > Mo(IV) can reduce > Fe(III) with the formation of > Mo(VI) and > Fe(II) in $Fe_{0.36}Mo_{0.64}S_2$, and the as-generated Fe(II) is essential for the continued production of $SO_4^{\cdot -}$. The high catalytic performance of $Fe_{0.36}Mo_{0.64}S_2$ was interpreted by DFT calculations *via* strong Fe metal atoms-MoS_2 support interactions and the low formal oxidation state of Fe in $Fe_{0.36}Mo_{0.64}S_2$. Thus, $Fe_xMo_{1-x}S_2$, with synergistic Fe and Mo sites, is a versatile, efficient and stable catalyst in practical AOP-based water treatment processes.

CRediT authorship contribution statement

Li-Zhi Huang: Conceptualization, Methodology, Writing - original draft, Project administration, Funding acquisition. **Chu Zhou:** Validation, Investigation. **Miaolong Shen:** Validation, Investigation. **Enlai Gao:** Formal analysis. **Chunbo Zhang:** Formal analysis. **Xin-Ming Hu:** Writing - review & editing. **Yiqun Chen:** Supervision, Funding acquisition. **Yingwen Xue:** Supervision. **Zizheng Liu:** Supervision, Funding acquisition.

Declaration of Competing Interest

The authors declare that they have no known competing financial interests or personal relationships that could have appeared to influence the work reported in this paper.

Acknowledgements

This work was funded by the National Natural Science Foundation

of China (Grant No. 51978537, 41807188, 51508423 and 51508423), the National Natural Science Foundation of China and the Russian Foundation for Basic Research (NSFC–RFBR 51811530099).

Appendix A. Supplementary data

Supplementary material related to this article can be found, in the online version, at doi:https://doi.org/10.1016/j.jhazmat.2020.122137.

References

Ahmad, M., Teel, A.L., Watts, R.J., 2013. Mechanism of persulfate activation by phenols. Environ. Sci. Technol. 47, 5864–5871.

An, S., Zhang, G., Wang, T., Zhang, W., Li, K., Song, C., Miller, J.T., Miao, S., Wang, J., Guo, X., 2018. High-density ultra-small clusters and single-atom Fe sites embedded in graphitic carbon nitride (g-C_3N_4) for highly efficient catalytic advanced oxidation processes. ACS Nano 12, 9441–9450.

Blöchl, P.E., 1994. Projector augmented-wave method. Phys. Rev. B 50, 17953.

Chakma, S., Moholkar, V.S., 2014. Investigations in synergism of hybrid advanced oxidation processes with combinations of sonolysis + Fenton process + UV for degradation of bisphenol A. Ind. Eng. Chem. Res. 53, 6855–6865.

Chang, K., Chen, W., 2011. L-cysteine-assisted synthesis of layered MoS_2/graphene composites with excellent electrochemical performances for lithium ion batteries. ACS Nano 5, 4720–4728.

Chen, F., Jiang, X., Zhang, L., Lang, R., Qiao, B., 2018. Single-atom catalysis: bridging the homo- and heterogeneous catalysis. Chin. J. Catal. 39, 893–898.

Deng, J., Li, H., Xiao, J., Tu, Y., Deng, D., Yang, H., Tian, H., Li, J., Ren, P., Bao, X., 2015. Triggering the electrocatalytic hydrogen evolution activity of the inert two-dimensional MoS_2 surface via single-atom metal doping. Energy Environ. Sci. 8, 1594–1601.

Furman, O.S., Teel, A.L., Watts, R.J., 2010. Mechanism of base activation of persulfate. Environ. Sci. Technol. 44, 6423–6428.

Guo, Z., Xie, Y., Xiao, J., Zhao, Z.-J., Wang, Y., Xu, Z., Zhang, Y., Yin, L., Cao, H., Gong, J., 2019. Single-atom Mn–N_4 site-catalyzed peroxone reaction for the efficient production of hydroxyl radicals in an acidic solution. J. Am. Chem. Soc. 141, 12005–12010.

Henkelman, G., Arnaldsson, A., Jonsson, H., 2006. A fast and robust algorithm for Bader decomposition of charge density. Comput. Mater. Sci. 36, 354–360.

Huang, Y.F., Huang, Y.H., 2009. Behavioral evidence of the dominant radicals and intermediates involved in Bisphenol A degradation using an efficient Co^{2+}/PMS oxidation process. J. Hazard. Mater. 167, 418–426.

Huang, L.-Z., Ayala-Luis, K.B., Fang, L., Dalby, K.N., Kasama, T., Bender Koch, C., Hansen, H.C.B., 2013. Oxidation of dodecanoate intercalated iron(II)–iron(III) layered double hydroxide to form 2D iron(III) (hydr)oxide layers. Eur. J. Inorg. Chem. 2013, 5718–5727.

Huang, L.Z., Pedersen, S.U., Bjerglund, E.T., Lamagni, P., Glasius, M., Hansen, H.C.B., Daasbjerg, K., 2017. Hierarchical MoS_2 nanosheets on flexible carbon felt as an efficient flow-through electrode for dechlorination. Environ. Sci.-Nano 4, 2286–2296.

Johnson, R.L., Tratnyek, P.G., Johnson, R.O.B., 2008. Persulfate persistence under thermal activation conditions. Environ. Sci. Technol. 42, 9350–9356.

Jones, J., Xiong, H., DeLaRiva, A.T., Peterson, E.J., Hien, P., Challa, S.R., Qi, G., Oh, S., Wiebenga, M.H., Hernandez, X.I.P., Wang, Y., Datye, A.K., 2016. Thermally stable single-atom platinum-on-ceria catalysts via atom trapping. Science 353, 150–154.

Kim, C., Ahn, J.-Y., Kim, T.Y., Shin, W.S., Hwang, I., 2018. Activation of persulfate by nanosized zero-valent iron (NZVI): mechanisms and transformation products of NZVI. Environ. Sci. Technol. 52, 3625–3633.

Kresse, G., Furthmüller, J., 1996. Efficient iterative schemes for ab initio total-energy calculations using a plane-wave basis set. Phys. Rev. B 54, 11169.

Kresse, G., Hafner, J., 1994. Ab initio molecular-dynamics simulation of the liquid-metal–amorphous-semiconductor transition in germanium. Phys. Rev. B 49, 14251.

Lee, M., Merle, T., Rentsch, D., Canonica, S., von Gunten, U., 2017. Abatement of polychoro-1,3-butadienes in aqueous solution by ozone, UV photolysis, and advanced oxidation processes (O_3/H_2O_2 and UV/H_2O_2). Environ. Sci. Technol. 51, 497–505.

Li, X., Bi, W., Zhang, L., Tao, S., Chu, W., Zhang, Q., Luo, Y., Wu, C., Xie, Y., 2016. Single-atom Pt as co-catalyst for enhanced photocatalytic H_2 evolution. Adv. Mater. 28, 2427–2431.

Li, X.N., Huang, X., Xi, S.B., Miao, S., Ding, J., Cai, W.Z., Liu, S., Yang, X.L., Yang, H.B., Gao, J.J., Wang, J.H., Huang, Y.Q., Zhang, T., Liu, B., 2018. Single cobalt atoms anchored on porous N-doped graphene with dual reaction sites for efficient Fenton-like catalysis. J. Am. Chem. Soc. 140, 12469–12475.

Lin, J., Wang, A., Qiao, B., Liu, X., Yang, X., Wang, X., Liang, J., Li, J., Liu, J., Zhang, T., 2013. Remarkable performance of Ir_1/FeO_x single-atom catalyst in water gas shift reaction. J. Am. Chem. Soc. 135, 15314–15317.

Liu, H., Bruton, T.A., Doyle, F.M., Sedlak, D.L., 2014. In situ chemical oxidation of contaminated groundwater by persulfate: decomposition by Fe(III)- and Mn(IV)-containing oxides and aquifer materials. Environ. Sci. Technol. 48, 10330–10336.

Liu, W., Zhang, L., Yan, W., Liu, X., Yang, X., Miao, S., Wang, W., Wang, A., Zhang, T., 2016. Single-atom dispersed Co-N-C catalyst: structure identification and performance for hydrogenative coupling of nitroarenes. Chem. Sci. 7, 5758–5764.

Liu, J., Dong, C., Deng, Y., Ji, J., Bao, S., Chen, C., Shen, B., Zhang, J., Xing, M., 2018. Molybdenum sulfide Co-catalytic Fenton reaction for rapid and efficient inactivation of Escherichia colis. Water Res. 145, 312–320.

Luo, Z., Ouyang, Y., Zhang, H., Xiao, M., Ge, J., Jiang, Z., Wang, J., Tang, D., Cao, X., Liu, C., Xing, W., 2018. Chemically activating MoS_2 *via* spontaneous atomic palladium interfacial doping towards efficient hydrogen evolution. Nat. Commun. 9, 2120.

Matzek, L.W., Tipton, M.J., Farmer, A.T., Steen, A.D., Carter, K.E., 2018. Understanding electrochemically activated persulfate and its application to ciprofloxacin abatement. Environ. Sci. Technol. 52, 5875–5883.

Miao, J., Xiao, F.-X., Yang, H.B., Khoo, S.Y., Chen, J., Fan, Z., Hsu, Y.-Y., Chen, H.M., Zhang, H., Liu, B., 2015. Hierarchical Ni-Mo-S nanosheets on carbon fiber cloth: a flexible electrode for efficient hydrogen generation in neutral electrolyte. Sci. Adv. 1.

Monkhorst, H.J., Pack, J.D., 1976. Special points for Brillouin-zone integrations. Phys. Rev. B 13, 5188.

Pei, G.X., Liu, X.Y., Wang, A., Lee, A.F., Isaacs, M.A., Li, L., Pan, X., Yang, X., Wang, X., Tai, Z., Wilson, K., Zhang, T., 2015. Ag alloyed Pd single-atom catalysts for efficient selective hydrogenation of acetylene to ethylene in excess ethylene. ACS Catal. 5, 3717–3725.

Perdew, J.P., Burke, K., Ernzerhof, M., 1996. Generalized gradient approximation made simple. Phys. Rev. Lett. 77, 3865–3868.

Qiu, H.J., Ito, Y., Cong, W., Tan, Y., Liu, P., Hirata, A., Fujita, T., Tang, Z., Chen, M., 2015. Nanoporous graphene with single-atom nickel dopants: an efficient and stable catalyst for electrochemical hydrogen production. Angew. Chem.-Int. Ed. 54, 14031–14035.

Raebiger, H., Lany, S., Zunger, A., 2008. Charge self-regulation upon changing the oxidation state of transition metals in insulators. Nature 453, 763–766.

Ren, Y., Lin, L., Ma, J., Yang, J., Feng, J., Fan, Z., 2015. Sulfate radicals induced from peroxymonosulfate by magnetic ferrospinel MFe2O4 (M = Co, Cu, Mn, and Zn) as heterogeneous catalysts in the water. Appl. Catal. B 165, 572–578.

Rong, X., Xie, M., Kong, L., Natarajan, V., Ma, L., Zhan, J., 2019. The magnetic biochar derived from banana peels as a persulfate activator for organic contaminants degradation. Chem. Eng. J. 372, 294–303.

Sun, T., Xu, L., Wang, D., Li, Y., 2019. Metal organic frameworks derived single atom catalysts for electrocatalytic energy conversion. Nano Res. 12, 2067–2080.

Wang, Y., Mao, J., Meng, X., Yu, L., Deng, D., Bao, X., 2019. Catalysis with two-dimensional materials confining single atoms: concept, design, and applications. Chem. Rev. 119, 1806–1854.

Xing, M., Xu, W., Dong, C., Bai, Y., Zeng, J., Zhou, Y., Zhang, J., Yin, Y., 2018. Metal sulfides as excellent co-catalysts for H_2O_2 decomposition in advanced oxidation processes. Chem 4, 1359–1372.

Xu, L., Yang, L., Bai, X., Du, X., Wang, Y., Jin, P., 2019. Persulfate activation towards organic decomposition and Cr(VI) reduction achieved by a novel CQDs-TiO_{2-x}/rGO nanocomposite. Chem. Eng. J. 373, 238–250.

Yan, H., Cheng, H., Yi, H., Lin, Y., Yao, T., Wang, C., Li, J., Wei, S., Lu, J., 2015. Single-atom Pd-1/graphene catalyst achieved by atomic layer deposition: remarkable performance in selective hydrogenation of 1,3-butadiene. J. Am. Chem. Soc. 137, 10484–10487.

Yin, P., Yao, T., Wu, Y., Zheng, L., Lin, Y., Liu, W., Ju, H., Zhu, J., Hong, X., Deng, Z., Zhou, G., Wei, S., Li, Y., 2016. Single cobalt atoms with precise N-coordination as superior oxygen reduction reaction catalysts. Angew. Chem.-Int. Ed. 55, 10800–10805.

Yin, Y., Shi, L., Li, W., Li, X., Wu, H., Ao, Z., Tian, W., Liu, S., Wang, S., Sun, H., 2019. Boosting Fenton-like reactions *via* single atom Fe catalysis. Environ. Sci. Technol.

Zeng, H., Zhao, X., Zhao, F., Park, Y., Sillanpää, M., 2019. Accelerated Fe^{3+}/Fe^{2+} cycle using atomic H* on Pd/Al_2O_3: a novel mechanism for an electrochemical system with particle electrode for iron sludge reduction in the Fe^{2+}/peroxydisulfate oxidation process. Chem. Eng. J., 122972.

Zhang, T., Zhu, H., Croué, J.-P., 2013. Production of sulfate radical from peroxymonosulfate induced by a magnetically separable $CuFe_2O_4$ spinel in water: efficiency, stability, and mechanism. Environ. Sci. Technol. 47, 2784–2791.

Zhang, H., Liu, G., Shi, L., Ye, J., 2018. Single-atom catalysts: emerging multifunctional materials in heterogeneous catalysis. Adv. Energy Mater. 8.

Zhou, Z., Liu, X., Sun, K., Lin, C., Ma, J., He, M., Ouyang, W., 2019. Persulfate-based advanced oxidation processes (AOPs) for organic-contaminated soil remediation: a review. Chem. Eng. J. 372, 836–851.

Zhou, H., Lai, L., Wan, Y., He, Y., Yao, G., Lai, B., 2020. Molybdenum disulfide (MoS_2): a versatile activator of both peroxymonosulfate and persulfate for the degradation of carbamazepine. Chem. Eng. J. 384, 123264.

Supplementary information for

Persulfate activation by two-dimensional MoS_2 confining single Fe atoms: performance, mechanism and DFT calculations

Li-Zhi Huang[a], Chu Zhou[a], Miaolong Shen[a], Enlai Gao[a], Chunbo Zhang[a], Xin-Ming Hu[b], Yiqun Chen [a,*], Yingwen Xue [a], Zizheng Liu[a,*]

[a] *School of Civil Engineering, Wuhan University, No. 8, East Lake South Road, Wuhan 430072, China*

[b] *Carbon Dioxide Activation Center, Interdisciplinary Nanoscience Center (iNANO) and Department of Chemistry, Aarhus University, Gustav Wieds Vej 14, DK-8000, Aarhus C, Denmark*

* Corresponding authors: yq.chen@whu.edu.cn (Y. Chen); lzz2015@whu.edu.cn (Z. Liu)

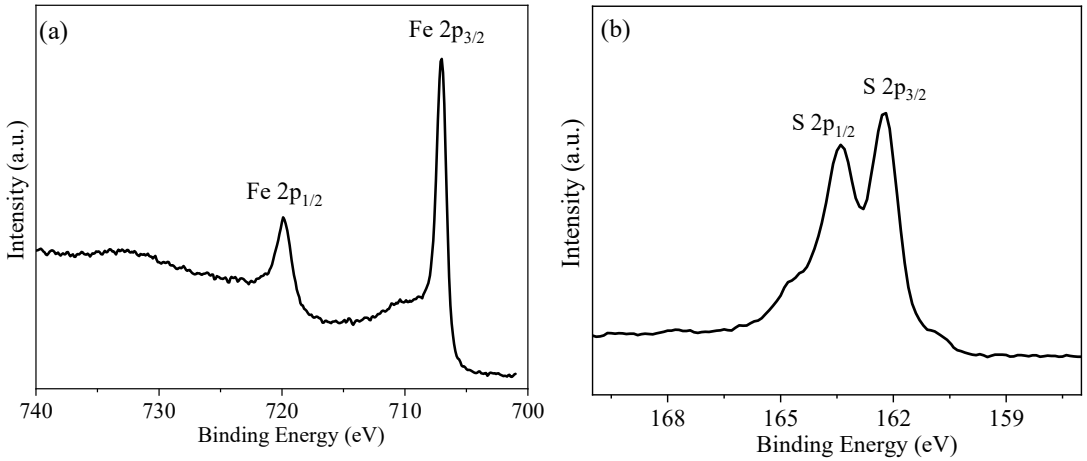

Figure S 1. High resolution Fe2p and S2p spectra of as-synthesized FeS reference catalyst.

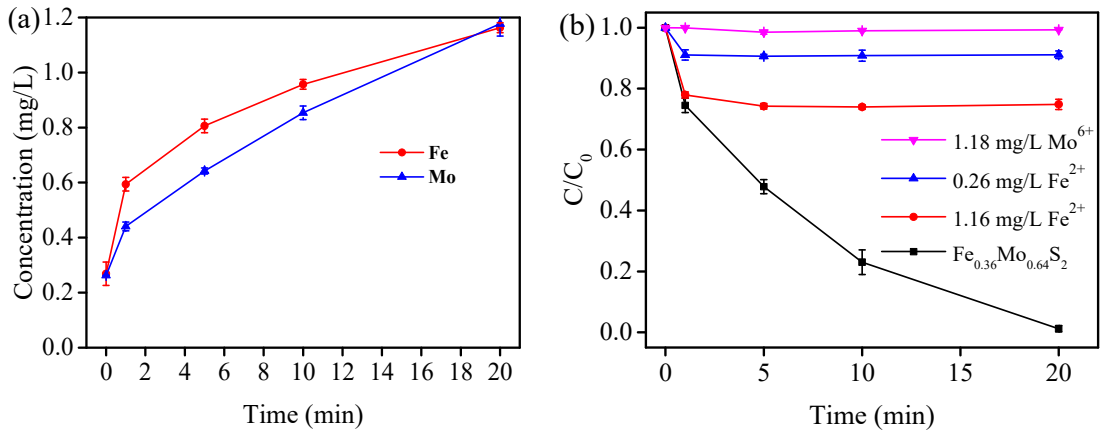

Figure S 2. (a) Dissolution of Fe and Mo ions during reaction course (b) Degradation of aniline in homogeneous system. $[Fe_{0.36}Mo_{0.64}S_2]_0$ = 0.1 g L^{-1}, $[PS]_0$ = 1 mM, $[Aniline]_0$ = 10 μM, pH 4.0.

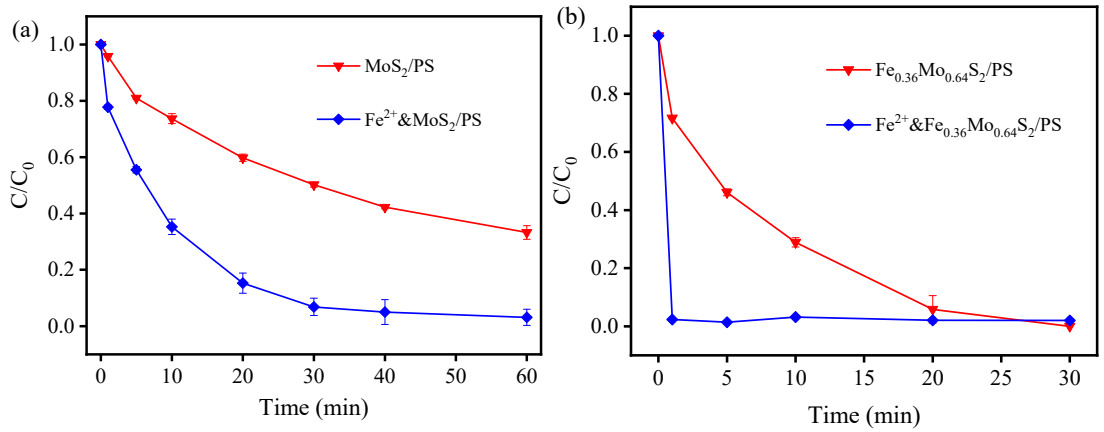

Figure S 3. Effect of dissolved Fe^{2+} on aniline degradation in MoS_2/PS (a) and $Fe_{0.36}Mo_{0.64}S_2$/PS (b) systems. Added $[Fe^{2+}]$=1.16 mg/L, $[MoS_2]=[Fe_{0.36}Mo_{0.64}S_2]_0$ = 0.1 g L^{-1}, $[PS]_0$ = 1 mM, $[Aniline]_0$ = 10 μM, pH 4.0. The concentration of Fe^{2+} in (b) could be double the concentration in (a) due to the release of Fe from $Fe_{0.36}Mo_{0.64}S_2$. Subsequently, the addition of the same amount of Fe^{2+} may resulted in much greater enhancement in $Fe_{0.36}Mo_{0.64}S_2$/PS system than MoS_2/PS system.

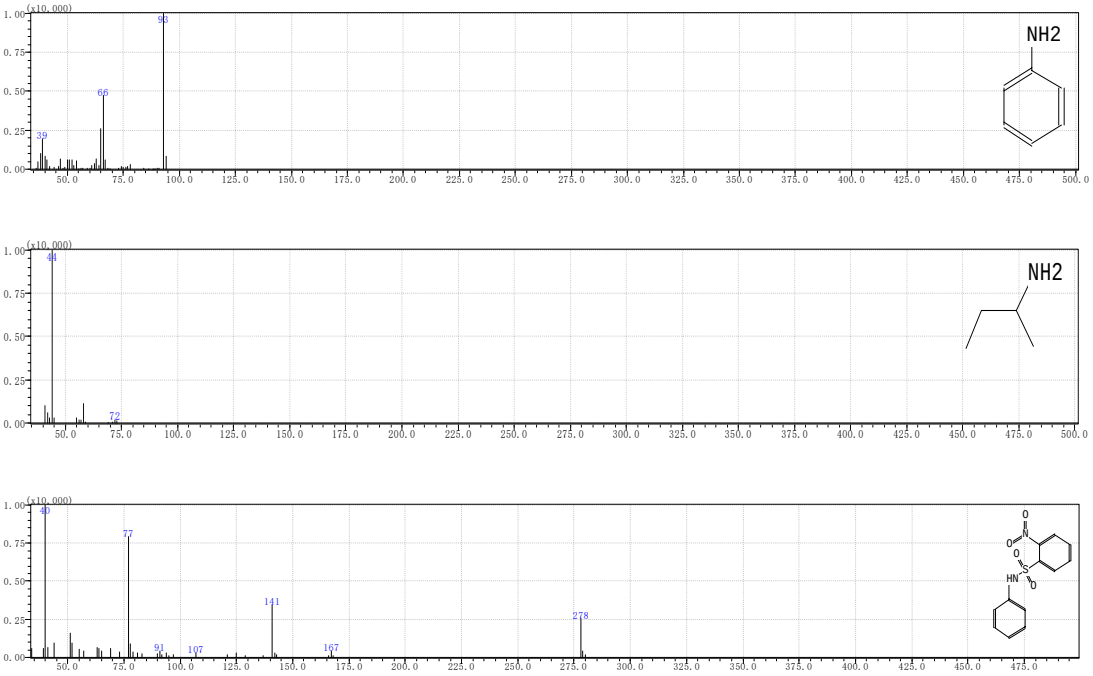

Figure S 4. Aniline and possible degradation products observed by GC-MS.

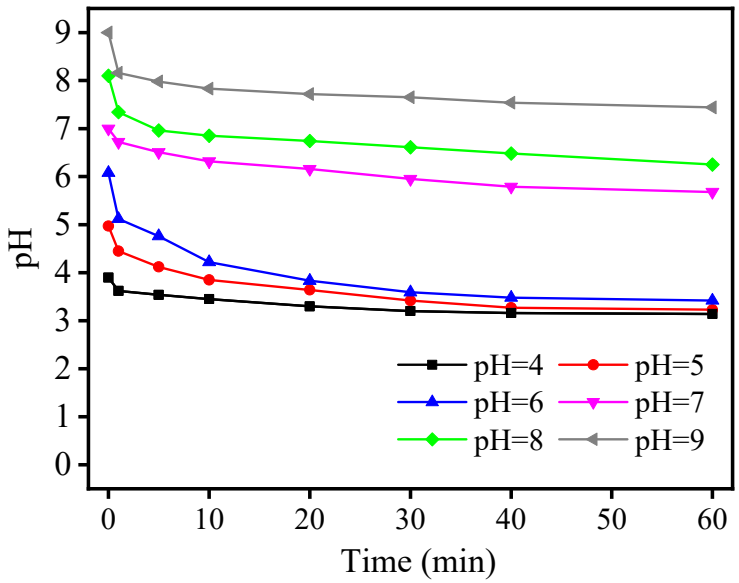

Figure S 5. Change of pH with different initial pH during the reaction course. $[Aniline]_0$=10 μM, $Fe_{0.36}Mo_{0.64}S_2$ dosage = 0.1 g/L, $[PS]_0$=1mM.

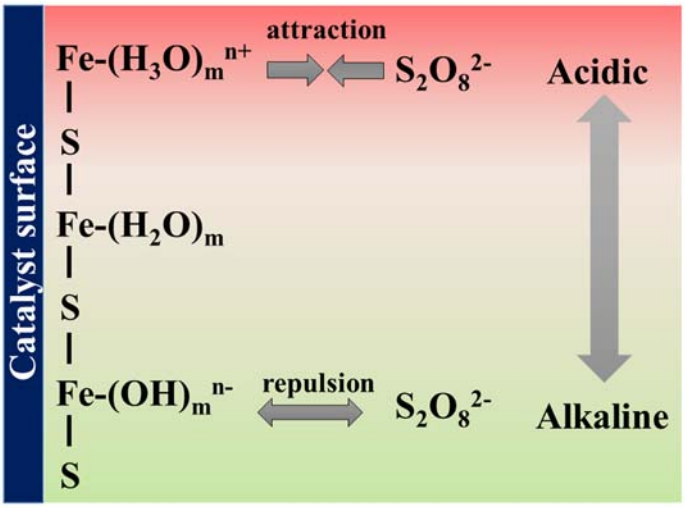

Figure S 6. Distribution of Fe species on $Fe_{0.36}Mo_{0.64}S_2$ catalyst surface at different pHs.

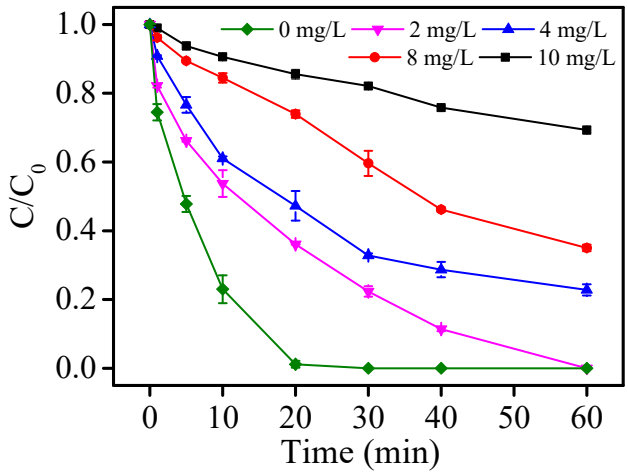

Figure S 7. Influence of humic acid on aniline degradation in $Fe_{0.36}Mo_{0.64}S_2$/PS system $[Aniline]_0$=10 μM, $[PS]_0$=1mM, $[humic\ acid]_0$ = 0–10 mM, pH=4.0. The inhibiting effect of humic acid on the system is mainly due to the fact that its structure contains large number of aromatic and aliphatic rings with carboxyl, hydroxyl and carbonyl functional groups, which can be easily attacked by $SO_4^{\bullet-}$

and HO• radicals. Humic acid compete with AN for radicals andthus inhibits AN degradation in $Fe_xMo_{1-x}S_2$/PS system.

Table S 1. HPLC analysis methods for organic pollutants

Organic pollutants	Eluent (v/v)	Injection volume (μL)	Flow rate (mL/min)	Absorption (nm)
aniline	Methanol/water=30/70	100	1	220
estriol (E3)	Methanol/water=40/60	100	1	280
benzoic acid	Methanol/water=50/50	100	1	227
p-chlorobenzoic acid	Acetonitrile/water=50/50	100	1	234
nitrobenzene	Acetonitrile/water=45/55	100	1	254
Propranolol	Acetonitrile/water=40/60	100	1	230

[a]

[a]Consist of 10mM K_2HPO_4.

Table S 2. Water quality of water sampled from East Lake

Total organic carbon ($mg \cdot L^{-1}$)	Total nitrogen ($mg \cdot L^{-1}$)	Total phosphorus ($mg \cdot L^{-1}$)	UV254	pH
33.38	0.89	0.08	0.013	8.52

Table S 3. Charge transfer of Fe atoms in $Fe_{0.36}Mo_{0.64}S_2$, FeO and Fe_2O_3.

Atoms	$Fe_{0.36}Mo_{0.64}S_2$	FeO	Fe_2O_3
Fe	–0.6779	–1.3205	–1.3764